

Deep learning of committor for ion dissociation and interpretable analysis of solvent effects using atom-centered symmetry functions

Kenji Okada,¹ Kazushi Okada,¹ Kei-ichi Okazaki,^{2,3,a)} Toshifumi Mori,^{4,5,b)} Kang Kim,^{1,c)} and Nobuyuki Matubayasi^{1,d)}

¹⁾Division of Chemical Engineering, Department of Materials Engineering Science, Graduate School of Engineering Science, The University of Osaka, Toyonaka, Osaka 560-8531, Japan

²⁾Research Center for Computational Science, Institute for Molecular Science, Okazaki, Aichi 444-8585, Japan

³⁾Graduate Institute for Advanced Studies, SOKENDAI, Okazaki, Aichi 444-8585, Japan

⁴⁾Institute for Materials Chemistry and Engineering, Kyushu University, Kasuga, Fukuoka 816-8580, Japan

⁵⁾Interdisciplinary Graduate School of Engineering Sciences, Kyushu University, Kasuga, Fukuoka 816-8580, Japan

(Dated: 10 February 2026)

The association and dissociation of ion pairs in water are fundamental to physical chemistry, yet their reaction coordinates are complex, involving not only interionic distance but also solvent-mediated hydration structures. These processes are often represented by free-energy landscapes constructed from collective variables (CVs), such as interionic distance and water bridging structures; however, it remains uncertain whether such representations reliably capture the transition pathways between the two associated and dissociated states. In this study, we employ deep learning to identify reaction coordinates for NaCl ion pair association and dissociation in water, using the committor as a quantitative measure of progress along the transition pathway through the transition state. The solvent environment surrounding the ions is encoded through descriptors based on atom-centered symmetry functions (ACSFs), which serve as input variables for the neural network. In addition, Shapley Additive exPlanations analysis, as an explainable artificial intelligence technique, is applied to identify ACSFs that contribute to the reaction coordinate. A comparative analysis of their correlation with CVs representing water bridging structures, such as interionic water density and the number of water molecules coordinating both ions, further provides a molecular-level interpretation of the ion association-dissociation mechanism in water.

I. INTRODUCTION

To understand transition processes involving many degrees of freedom in complex molecular systems, such as ion dissociation and isomerization, it is essential to examine the corresponding free-energy landscape.¹⁻⁴ From the system's total degrees of freedom, a collective variable (CV) X , for example, an interatomic distance, bond angle, or dihedral angle, is conventionally employed. The free-energy landscape can be described by the potential of mean force (PMF), $-k_B T \ln P(X)$, where $P(X)$ denotes the probability distribution function with respect to X . When the resulting PMF exhibits two minima separated by a saddle point, these minima correspond to distinct stable states, while the transition pathway is expected to pass in the vicinity of the saddle point. In this context, the saddle point represents the transition state (TS), and the CV X can be regarded as the reaction coordinate (RC). However, a fundamental difficulty arises in that the selection of X is arbitrary.

A method known as committor analysis is commonly used to evaluate CV as an appropriate RC.⁵⁻¹³ The committor, p_B^* , is defined as the probability that a trajectory initiated from a

given configuration reaches the product state B before reaching the reactant state A. A value of $p_B^* \approx 0$ indicates that the configuration lies near state A, whereas $p_B^* \approx 1$ signifies proximity to state B. Configurations for which $p_B^* = 0.5$ correspond to the TS ensemble. When a CV is chosen such that configurations with $p_B^* = 0.5$ coincide with the saddle point on the PMF, that CV can be regarded as the appropriate RC. However, because a large number of possible CVs exist and the evaluation is typically performed by trial and error, an automated and systematic approach is required.¹⁴

Machine learning approaches based on committor analysis have shown considerable promise for identifying RC, leading to the development of various methodological frameworks.¹⁵⁻³⁶ Recently, we developed a deep learning framework trained on committor values p_B^* of configurations sampled near the saddle point region from molecular dynamics (MD) simulations.³⁷ In this approach, candidate CVs are employed as input features, and the corresponding RC is predicted as the output variable through the neural network using p_B^* as the learning target. Because deep learning models often behave as black boxes, eXplainable AI (XAI) techniques are further employed to quantify the contribution of each input variable to the predicted RC. This approach enables the identification of CVs with significant contribution, providing a representation of the TS on the PMF that is consistent with the underlying transition pathways.

As an application, we previously investigated the isomerization reaction of alanine dipeptide and identified dihedral angles that primary contributor to the RC.³⁷ Furthermore, we

^{a)}Electronic mail: keokazaki@ims.ac.jp

^{b)}Electronic mail: toshi_mori@cm.kyushu-u.ac.jp

^{c)}Electronic mail: kk@cheng.es.osaka-u.ac.jp

^{d)}Electronic mail: nobuyuki@cheng.es.osaka-u.ac.jp

demonstrated that the isomerization can be characterized not only by the dihedral angles but also by specific interatomic distances.³⁸ We also investigated how hyperparameter tuning in the neural network model influences the performance and reliability of the identified RC.³⁹

In this study, we applied an explainable deep learning-based analytical framework for identifying appropriate CVs serving as RC to the association and dissociation process of NaCl ion pair in water. This process may appear to be described adequately by the interionic distance r_{ion} .^{40–47} Geissler *et al.* applied committor analysis to the dissociation of a NaCl ion pair in water.⁴⁸ They constructed a TS ensemble by constraining r_{ion} to the saddle point region of the PMF. The resulting distribution of the committor p_{B}^* was bimodal, with pronounced peaks at $p_{\text{B}}^* = 0$ and $p_{\text{B}}^* = 1$, while the distribution near $p_{\text{B}}^* = 0.5$ was relatively low. This result indicated r_{ion} alone does not fully capture the TS along the RC. They further examined the structural features of the solvent environment surrounding the ions for configurations with $p_{\text{B}}^* = 0$ and $p_{\text{B}}^* = 1$. The analysis showed that Na ions were predominantly five coordinated at $p_{\text{B}}^* = 0$, whereas six coordination dominated at $p_{\text{B}}^* = 1$. In contrast, no substantial change was observed in the coordination environment of Cl ions. These findings suggest that the dissociation process involves an increase in the coordination number of Na ions from the associated to the dissociated state.

Furthermore, Bellard and Dellago performed committor analysis, in which both r_{ion} and water molecules were constrained.⁴⁹ In their approach, water molecules were restricted by varying the probe region surrounding the ions, and the resulting committor distributions were examined. The results showed that, as the constrained region was extended from the first to the third coordination shell, the committor distribution progressively sharpened around $p_{\text{B}}^* = 0.5$. This result demonstrated that ion pair dissociation is closely associated with solvent motion between the second and third solvation shells.

Here, particular attention is devoted to the construction of CVs that describe water molecules surrounding ions.^{28,50–58} Müllen *et al.* calculated a total of 71 CVs, including the local density of solvent molecules or atoms relative to the ion pair such as first and second shell coordination numbers, interionic water density, energy gaps, and other electrostatic descriptors.⁵⁰ Then, the combinations of up to three CVs were employed in the Inertial Likelihood Maximization method.⁵⁹ In particular, CVs such as the interionic water density and the water molecules simultaneously coordinating both ions were identified as important.

Jung *et al.* developed a committor based machine learning approach combined with symbolic regression and applied it to various systems, including ion dissociation in water.²⁸ They employed atom-centered symmetry functions (ACSFs), widely used as descriptors in machine learning potentials,^{60–62} as CVs. Specifically, they incorporated ACSFs to describe the geometric structures of water O and H atoms surrounding cations and anions. Symbolic regression enables the RC identified by neural network learning of the committor p_{B}^* to be expressed as explicit functional forms of the primary contributing CVs, including the ACSFs that describe the structure

of water O atoms around the cations.

In this study, we aim to enhance interpretability of ACSF-based committor models trained by a neural network. In particular, we employ SHapley Additive exPlanations (SHAP), a game-theory-based method that decomposes a trained model prediction into additive contributions from individual input features.⁶³ Here, SHAP is used to assess the relative importance of candidate CVs and to elucidate how they contribute to the committor prediction learned by the neural network. Our primary objective is not the derivation of an explicit functional form relating the input variables to the prediction, but rather the physical interpretation of the ACSFs highlighted by the SHAP analysis. In this sense, our approach complements existing efforts based on symbolic regression, going beyond the derivation of compact analytical expressions by focusing on the physical meaning and mutual consistency of the contributing ACSFs. To this end, we perform a comparative analysis between the ACSFs emphasized by SHAP and conventional CVs, such as the interionic water density and the number of water molecules that simultaneously coordinate both ions, introduced in previous studies. This approach allows us to examine consistency with existing physical understanding, clarify differences, and extract additional insights afforded by the data-driven interpretation.

II. METHODS

A. MD simulations and committor evaluation

MD simulations were performed for NaCl ion pair in water. The system had a linear dimension of 40 Å and was simulated under periodic boundary conditions. It comprised one pair of Na and Cl ions by the AMBER99 force field⁶⁴ and 2048 TIP/4P-Ew⁶⁵ water molecules. Initially, MD simulations using the umbrella sampling method were performed at 300 K for 10 ns with the time step of 2 fs. A harmonic bias with a spring constant of $k = 500 \text{ kJ mol}^{-1} \text{ \AA}^{-2}$ was applied at 30 window positions spaced at 0.2 Å intervals over the interionic distance range from 2.2 Å to 8.0 Å. The temperature was controlled using the Nosé–Hoover thermostat. The real space cut-off length was set to 12 Å, and long range electrostatic interactions were evaluated using the particle mesh Ewald method. The potential of mean force (PMF) as a function of r_{ion} was then constructed using the WHAM method. The resulting PMF is illustrated in Fig. 1(a).

Next, an additional umbrella sampling was performed centered at $r_{\text{ion}} = 3.65 \text{ \AA}$ with a harmonic bias of a spring constant $k = 100 \text{ kJ mol}^{-1} \text{ \AA}^{-2}$. A total of 7600 configurations were extracted for interionic distances between $3.2 \text{ \AA} < r_{\text{ion}} < 4.3 \text{ \AA}$. This distance range was chosen to cover the saddle point position at $r_{\text{ion}} = 3.6 \text{ \AA}$ on the PMF, as shown in Fig. 1(a). The associated state A is defined for $r < 3.2 \text{ \AA}$, while the dissociated state B is defined for $r > 4.3 \text{ \AA}$. The committor p_{B}^* for each sampled configuration was evaluated by performing 100 independent 1 ps MD simulations at 300 K, each initialized with velocities randomly drawn from the Maxwell–Boltzmann distribution for the sampled configuration. The distribution of

the committor p_B^* is shown in Fig. 1(b). It can be seen that p_B^* tends toward 0 and 1, without exhibiting a pronounced peak near 0.5. This result is consistent with the findings of previous work,⁴⁸ indicating that the CV of r_{ion} is insufficient to account for the TS. All the MD simulations were performed using GROMACS 2024.5.⁶⁶

B. Neural network learning and SHAP

The neural network used in this study consists of five hidden layers, with the odd-numbered layers containing 400 nodes and even-numbered layers containing 200 nodes. The leaky rectified linear unit (Leaky ReLU) was used as the activation function, with the leaky parameter set to 0.01. Candidate CVs are provided as the input features, and the output is a one-dimensional variable q . The network is trained to regress the relationship between q and the committor p_B^* onto the sigmoid function $p_B(q) = (1 + \tanh(q))/2$. Consequently, q serves as the RC. The architecture of the neural network is same as that used in our previous studies.^{37,38}

The cross-entropy between $p_B(q) = (1 + \tanh(q))$ and p_B^* was employed as the loss function, which is expressed as

$$\mathcal{H}(p_B, p_B^*) = - \sum_k p_B^*(\mathbf{r}_k) \ln p_B(q) - \sum_k (1 - p_B^*(\mathbf{r}_k)) \ln [1 - p_B(q)], \quad (1)$$

where \mathbf{r}_k denotes the k -th initial configuration.^{21,67} This equation is derived from the Kullback–Leibler divergence, which quantifies the discrepancy between the distribution of the committor p_B^* and the expected committor function $p_B(q)$.⁶⁷ It is also noted that Eq. (1) represents a generalization of the log-likelihood function.¹⁷ The dataset of candidate CVs and committor p_B^* from 7600 configurations was partitioned into training, validation, and test datasets at a ratio of 5:1:4. Furthermore, overfitting was prevented using Dropout (probability 0.5) and L2 regularization (coefficient 0.001). Training was performed using the AdaMax optimizer with a batch size of 256 and a learning rate of 1×10^{-5} , over 4000 epochs. The epoch dependent loss functions of training and test datasets are shown in Fig. S1 of the Supplementary Material.

To enhance the interpretability of the neural network model, we employed the SHAP analysis as an XAI technique.⁶³ As described in the Introduction, SHAP quantifies the contribution of each input feature to the predictions, thereby providing an interpretable decomposition of feature contribution. In particular, SHAP employs an additive feature attribution framework using Shapley values based on game theory, ensuring a fair and consistent distribution of prediction values among input features. In the present study, this analysis is used to assess the relative importance of CVs for the committor prediction learned by the neural network. Note that while SHAP decomposes model predictions into additive feature contributions, it does not provide an explicit functional form of the relationship between the input variables and the prediction, which is instead addressed separately by symbolic regression.²⁸

C. Input features as candidate CVs

The ACSF describes how many atoms are located at specific distances and angles around a central atom.⁶¹ Owing to their invariance under translational and rotational operations, ACSFs provide a systematic and comprehensive representation of the solvent environment. Note that Geiger and Dellago proposed a machine learning method using ACSFs to classify the local structures of amorphous and crystalline structures.⁶⁸ Extended methods for identifying local structures in MD simulations, based on the neural network framework developed by Geiger and Dellago, have also been proposed.^{69,70}

To represent the solvent environment around the ions, we employed two types of ACSFs, G_i^2 and G_i^5 for reference atom i , as input variables for neural networks. These functions are defined as

$$G_i^{2,Z_1} = \sum_{j \neq i}^{|Z_1|} e^{-\eta(R_{ij}-R_s)^2} \cdot f_c(R_{ij}), \quad (2)$$

$$G_i^{5,Z_1,Z_2} = 2^{1-\zeta} \sum_{j \neq i}^{|Z_1|} \sum_{k \neq i}^{|Z_2|} (1 + \lambda \cos \theta_{ijk})^\zeta \cdot e^{-\eta((R_{ij}-R_s)^2 + (R_{ik}-R_s)^2)} \cdot f_c(R_{ij}) \cdot f_c(R_{ik}), \quad (3)$$

respectively. Note that R_{ij} (R_{ik}) represents the distance between atoms i and j (k), and θ_{ijk} denotes the angle formed by atoms j and k with atom i at the center. Z_1 and Z_2 represent atomic species surrounding the reference atom and the absolute value notation denotes their respective atomic numbers. Furthermore, the cut-off function is introduced as

$$f_c(R_{ij}) = \begin{cases} 0.5 \cdot [\cos(\pi R_{ij}/R_c) + 1] & \text{for } R_{ij} < R_c \\ 0 & \text{for } R_{ij} > R_c, \end{cases} \quad (4)$$

with the cut-off radius, R_c .

The ACSF G_i^2 is defined as the sum of a Gaussian function weighted by the cutoff function. The width of the Gaussian is determined by the parameter η , while its center can be positioned at a specific radial distance using the parameter R_s . This function is particularly suitable for characterizing the spherical shell environment surrounding a reference atom. The ACSF G_i^5 extends G_i^2 by incorporating an additional target atom and including an angular component. The parameter λ can take values of 1 or -1 , shifting the maximum of the cosine function to $\theta_{ijk} = 0^\circ$ and $\theta_{ijk} = 180^\circ$, respectively. The parameter ζ controls the angular resolution, with larger values of ζ corresponding to a narrower range of nonzero contributions in the ACSF.

As outlined in the Introduction, Jung *et al.* introduced ACSFs to describe the geometric structures of water O and H atoms around cations anions as candidate CVs in their machine learning analysis of the committor.²⁸ To consider CVs more comprehensively, we calculated all possible atomic combinations as follows: For G^2 , four combinations were used: $(i-Z_1) = (\text{Na-O}), (\text{Na-H}), (\text{Cl-O}), (\text{Cl-H})$. For G^5 , ten combinations were considered: $(Z_1-i-Z_2) = (\text{O-Na-O}), (\text{O-Na-H}), (\text{H-Na-H}), (\text{Cl-Na-H}), (\text{Cl-Na-O}), (\text{O-Cl-O}), (\text{O-Cl-H}),$

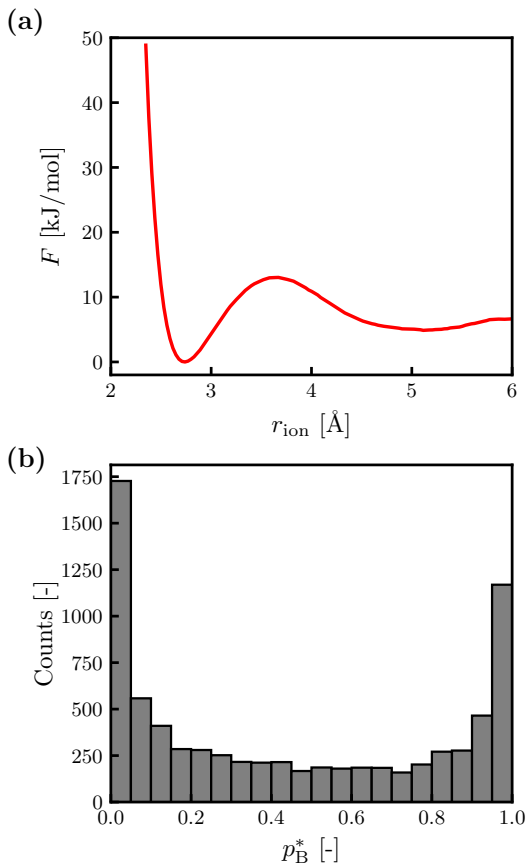


FIG. 1. (a) PMF $F(r_{\text{ion}})$ as a function the interionic distance r_{ion} . The point with the minimum energy is set to 0 kJ/mol. (b) Distribution of Committor p_{B}^* evaluated for configurations sampled within the range $3.2 \text{ \AA} < r_{\text{ion}} < 4.3 \text{ \AA}$.

(H-Cl-H), (Na-Cl-H), (Na-Cl-O). By systematically varying other parameters, R_s (ranging from 1 Å to 9 Å), λ (1 and -1), and ζ (1, 2, 4, 8, 16, 32, and 64), we generated a total of 1296 descriptors, comprising 36 G^2 and 1260 G^5 . The cutoff radius was fixed at $R_c = 10.0 \text{ \AA}$, with $\eta = 2.0 \text{ \AA}^{-2}$ for G^2 , and $\eta = 1.2 \text{ \AA}^{-2}$ for G^5 . Detailed definitions of the input features of two ACSFs, G^2 and G^5 , are provided in Tables S1 of the Supplementary Material. All input variables for the neural network were standardized.

III. RESULTS AND DISCUSSION

A. Predicted RC

We first present the result of the neural network training on the committor p_{B}^* . Figure 2(a) shows the relationship between p_{B}^* and q using the test data. The model performance was evaluated using two metrics: the coefficient of determination R^2 and the root-mean-square error (RMSE), which were found to be $(R^2, \text{RMSE}) = (0.766, 0.128)$. Our previous study investigated the isomerization of alanine dipeptides using the same neural network architecture; however, the present model

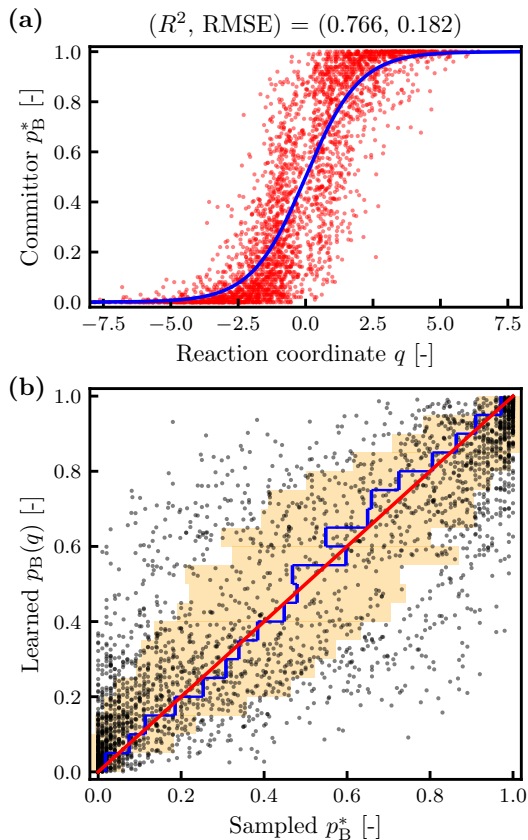


FIG. 2. (a) Relationship between committor p_{B}^* and the RC q predicted by the neural network trained model using the test dataset (3040 points). The blue curve represents the sigmoidal function, $p_{\text{B}}(q) = (1 + \tanh(q))/2$. (b) Comparison between the sampled committor p_{B}^* using the test dataset (3040 points) and the learned committor by the neural network. The vertical axis is divided into 20 bins; the mean of each bin shown as a blue line. The orange shaded area indicates the standard deviation, and the red line represents the identity.

exhibited slightly reduced predictive performance relative to the earlier one.^{37,38} This decrease is likely attributable to the substantial increase in degrees of freedom arising from the inclusion of solvent, although we consider the training to have been sufficiently converged.

Figure 2(b) compares the learned committor by the neural network with the sampled committor p_{B}^* . The close quantitative agreement between the two indicates the neural network accurately characterizes the reaction coordinate q , consistent with previous observations by Jung *et al.*²⁸ In addition, Fig. S2 of the supplementary material shows the distribution of p_{B}^* near the TS at $q = 0$. Using α as a threshold, the distribution of p_{B}^* within the range $|q| < \alpha$ increasingly exhibits a tendency to peak around 0.5 as α is reduced, although the peak is less sharply defined than that observed for the isomerization of alanine dipeptides.³⁷ Nevertheless, the predicted q obtained from the neural network model can serve as an appropriate RC for ion pair dissociation.

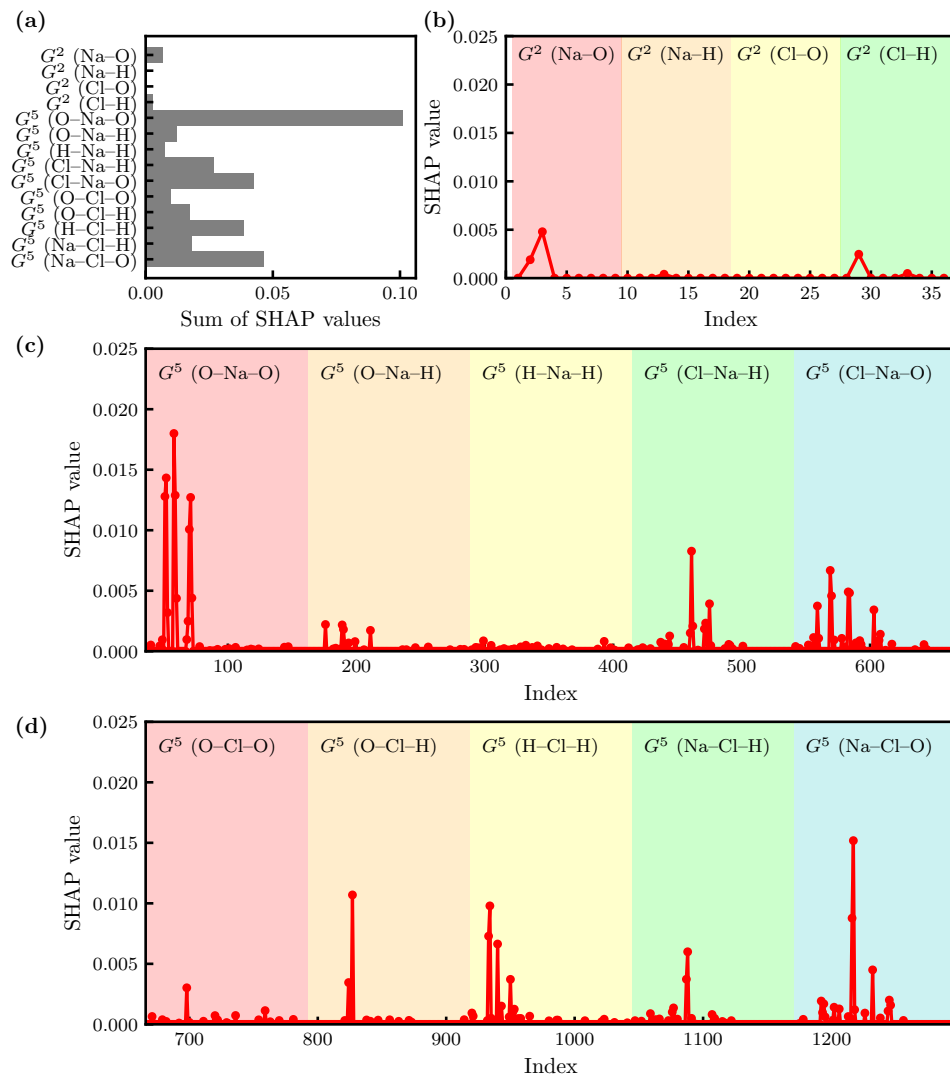


FIG. 3. Feature contribution of each CV evaluated by the absolute SHAP value. (a): Summed SHAP values for each atom combination (i - Z_1) in G^2 and (Z_1 - i - Z_2) in G^5 descriptors. (b): Index dependence of SHAP values for G^2 descriptors. (c) and (d): Index dependence of SHAP values for G^5 descriptors.

TABLE I. Top five dominant indices, those parameters, and absolute SHAP values among G^5 (O-Na-O) descriptors.

index	R_s [Å]	λ	ζ	absolute SHAP value
58	2.0	-1	1	0.0180
52	2.0	1	2	0.0143
59	2.0	-1	2	0.0129
51	2.0	1	1	0.0128
71	3.0	1	32	0.0127

TABLE II. Top five dominant indices, those parameters, and absolute SHAP values among G^5 (Na-Cl-O) descriptors.

index	R_s [Å]	λ	ζ	absolute SHAP value
1217	4.0	1	16	0.0152
1216	4.0	1	8	0.0088
1232	5.0	1	32	0.0045
1245	6.0	1	16	0.0020
1192	2.0	-1	1	0.0019

B. Feature contribution of CV by SHAP

The feature contribution of each input CV to the RC predicted by the neural network was evaluated using SHAP. The average of 100 SHAP values randomly sampled from the test dataset of 3040 configurations was calculated and the results

are plotted in Fig. 3.

Figure 3(a) shows the summed SHAP values for each atomic combination in the G^2 and G^5 descriptors. Overall, the contribution of G^2 is minimal, indicating that the information encoded in G^2 is effectively subsumed by the G^5 descriptors. Notably, within G^5 , (Z_1 - i - Z_2)=(O-Na-O) descriptors

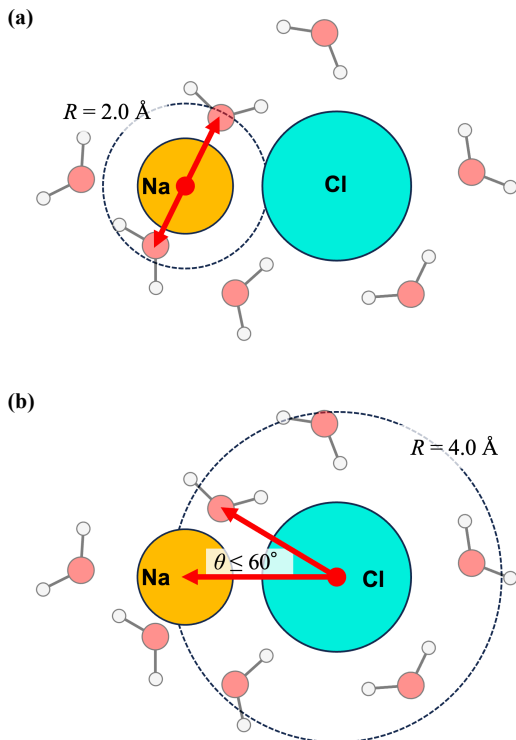


FIG. 4. Schematic illustration of water O atoms within 2 \AA of Na (a) and water O atoms within the 4 \AA hydration shell of Cl (b), characterized by two ACSF descriptors, G_{58}^5 and G_{1217}^5 , respectively.

exhibited the largest contribution, followed by (Na–Cl–O), (Cl–Na–O), and (H–Cl–H). This result indicates that the coordination of water O atoms around Na ion, as well as configurations involving one ion and a water O atom relative to the other ion, play a central role. Note that the environment of water O atoms surrounding both ions is common to the (Na–Cl–O) and (Cl–Na–O) descriptors. In contrast, the contribution of water H atoms around Cl ion is minor. This relatively minor contribution of solvation around Cl ion is consistent with the small change in the coordination number around Cl ion between the associated and dissociated states, as reported by Geissler *et al.*⁴⁸ Other descriptors, such as (Cl–Na–H) and (Na–Cl–H), which characterize water H atom around both ions, and (O–Na–H) and (O–Cl–H), which describe environments where O and H atoms coordinate around a single ion are found to be less important. These results suggest that the arrangement of H atoms around the ions is less significant than that of O atoms. Among the ten atom combinations, the (H–Na–H) and (O–Cl–O) descriptors, representing the coordination of water H and O atoms around Na and Cl ions, relatively, show the smallest contributions, consistent with the underlying electrostatic interactions.

Table I lists the top five contributors the within G^5 (O–Na–O) descriptors along with their corresponding absolute SHAP values. The G^5 descriptor at index 58 (denoted as G_{58}^5), corresponding to (O–Na–O) with the highest contribution, has the distance and angular sensitivities of $R_s = 2.0 \text{ \AA}$, $\lambda = -1$, and $\zeta = 1$. This indicates that water O atoms within

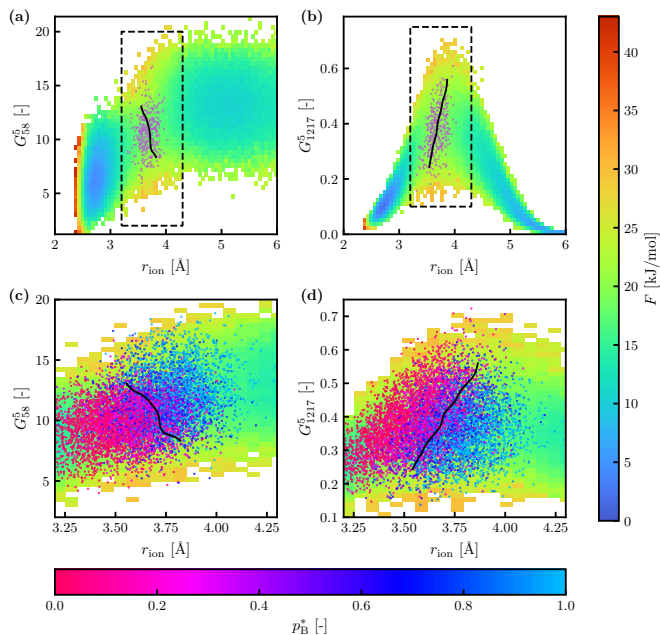


FIG. 5. Two-dimensional PMF using the interionic distance r_{ion} and G_{58}^5 (a) and G_{1217}^5 (b). The point with the minimum energy is set to 0 kJ/mol , and values are color-coded according to the color bar on the right. Purple dots indicate configurations with committer values in the range $0.45 < p_B^* < 0.55$. The distributions of committor p_B^* within the rectangular boxes in (a) and (b) are described in (c) and (d), respectively. Committer values are colored according to the bottom color bar. In each panel, the black contour line was obtained as follows: within the region in (c) or (d), corresponding the rectangular box in (a) or (b), the ranges of the x- and y-axis values were divided into 200 grid points each (forming a 200×200 grid), and the average committor value p_B^* within each grid cell was computed. After applying cubic interpolation for smoothing, the contour line corresponding to $p_B^* = 0.5$ was drawn.

a spherical shell of radius $R_s = 2.0 \text{ \AA}$ around Na make a significant contribution. This G_{58}^5 is largely consistent with the G^5 (denoted as x_7 in Ref. 28) with $R_s = 1.0 \text{ \AA}$, $\zeta = 2$ and $\lambda = -1$ identified by Jung *et al.* Note that $R_s = 2.0 \text{ \AA}$, which is slightly larger than that of x_7 , approximately corresponds to the Lennard-Jones diameter of Na ion. In contrast, the low angular resolution ($\zeta = 1$) suggests that angular dependence is not particularly important for characterizing the distribution of O atoms around Na ion. Typical structures are schematically illustrated in Fig. 4(a). The other descriptors listed in Table I exhibit similar properties, while their parameter values differ slightly.

In addition to G^5 (O–Na–O) descriptors, G^5 (Na–Cl–O) descriptors also make significant contributions to the RC. As listed in Table II, index 1217 (denoted as G_{1217}^5) contributes the most significantly, characterized by $R_s = 4.0 \text{ \AA}$, $\lambda = 1$, and $\zeta = 16$. At this high angular sensitivity ($\zeta = 16$), the angular component $2^{1-\zeta}(1 + \cos \theta_{ijk})^\zeta$ decreases from unity and approaches zero near $\theta_{ijk} \approx 60^\circ$, indicating that the dominant Na–Cl–O bond angles lie within this range. This implies that water O atoms located in the overlapping region of the

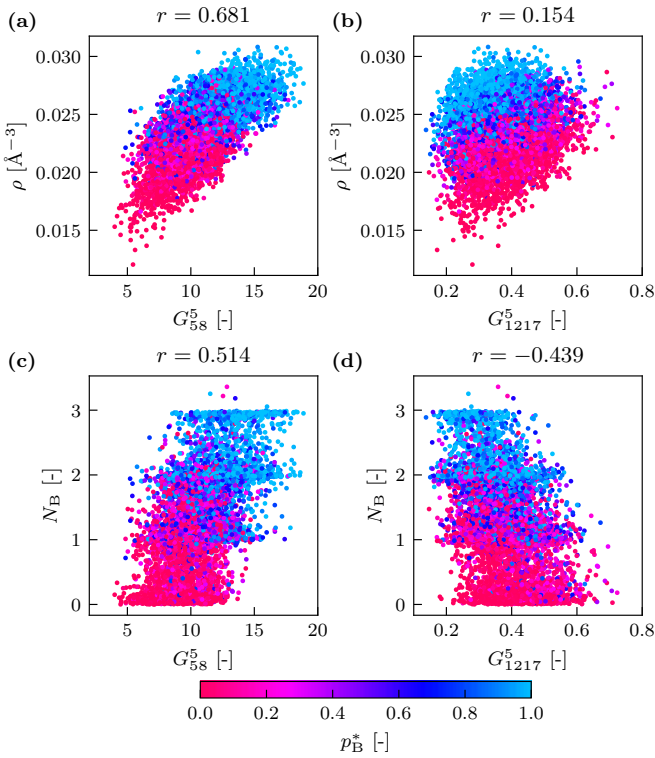


FIG. 6. Distribution of committor p_B^* dataset in the two-dimensional surface using the combinations (G_{58}^5, ρ) (a), (G_{1217}^5, ρ) (b), (G_{58}^5, N_B) (c), and (G_{1217}^5, N_B) (d). Committer values are colored according to the bottom color bar. The r -value represents the correlation coefficient for each panel.

hydration shells, corresponding to $R_s = 4 \text{ \AA}$ separation between Na and Cl ions, slightly larger than the saddle point distance $r_{\text{ion}} = 3.6 \text{ \AA}$ of the PMF, are key contributors [see the schematic illustration in Fig. 4(b)]. The other descriptors listed in Table II also imply similar structural features, except for index 1192.

It is important to characterize the p_B^* dataset using the interionic distance, r_{ion} , in combination with either of the two ACSF descriptors, G_{58}^5 or G_{1217}^5 , as shown in Fig. 5. Figures 5(a) and 5(b) display the two-dimensional PMFs constructed using $(r_{\text{ion}}, G_{58}^5)$ and $(r_{\text{ion}}, G_{1217}^5)$, respectively. The PMF was calculated using the `mbar_analysis` code⁷¹ in the GENESIS software,^{72–74} which implements the Multistate Bennett acceptance ratio method.⁷⁵ To examine the behavior near the TS, the distributions of p_B^* within the rectangular regions shown in Fig. 5(a) and 5(b) are presented in Figs. 5(c) and 5(d), respectively. These results demonstrate that the committor evolves continuously from the associated state ($p_B^* \approx 0$) to the dissociated state ($p_B^* \approx 1$), with the TS ($p_B^* = 0.5$) forming clear separatrix lines, which are consistent with the corresponding PMF profiles.

Specifically, Figs. 5(a) and 5(c) show that an increase in G_{58}^5 accompanied by an increase in r_{ion} leads to the crossing of the separatrix line, indicating that enhanced coordination of water O atoms around Na ion plays a crucial role for the ion pair dissociation. This observation is consistent with the finding by

Geissler *et al.* that the coordination number around the Na ion increases during the transition from the associated to the dissociated state.⁴⁸ Furthermore, Figs. 5(b) and 5(d) demonstrate that, starting from the associated state ($p_B \approx 0$), G_{1217}^5 initially increases together with r_{ion} as the system approaches the TS ($p_B = 0.5$). Upon crossing the separatrix line, however, G_{1217}^5 decreases as the system proceeds toward the dissociation state ($p_B \approx 1$). This behavior indicates that ion pair dissociation requires a reduction in the density of water O atoms that belong simultaneously to the hydration shells of both Na and Cl ions. Therefore, the two ACSF descriptors, G_{58}^5 and G_{1217}^5 , identified through the neural network and SHAP analysis, characterize the underlying mechanism of the dissociation process of NaCl ion pair in water. In particular, the separatrix lines shown in Fig. 5 imply that barrier crossing at the TS requires water molecules coordinating Na ion to migrate toward Cl ion, as pointed out by Geissler *et al.*⁴⁸

C. Comparative analysis with CVs representing water bridging structure

Finally, it is also important to examine the correlations of G_{58}^5 and G_{1217}^5 with CVs previously identified using the Inertial Likelihood Maximization method by Müller *et al.*⁵⁰ As described in the Introduction, the interionic water density ρ and the number of water molecules that simultaneously coordinate both ions, N_B were found to contribute most significantly to the RC. Specifically, the interionic water density ρ is defined by

$$\rho = \left(\frac{1}{2\pi\sigma^2} \right)^{3/2} \sum_w \exp\left(-\frac{|\mathbf{r}_w - \mathbf{r}_{\text{mid}}|^2}{2\sigma^2} \right), \quad (5)$$

where \mathbf{r}_w and \mathbf{r}_{mid} represent the center-of-mass position of the w -th water molecule and the midpoint between Na and Cl ions, respectively. The parameter σ controls the number of water molecules within the volume $(2\pi\sigma^3)^{1/2}$, which is chosen as $r_{\text{ion}}/2$. The number of water molecules that simultaneously coordinate both ions, N_B , is calculated based on the following two steps: The ion coordination function is defined as

$$f_{s-w} = \frac{1 - \tanh[a(R_{s-w} - b)]}{2}, \quad (6)$$

where the subscript s represents an ion species, *i.e.*, Na or Cl. The distance R_{s-w} corresponds to the w -th water O atom when calculating Na coordination, and to the w -th water H atom when calculating Cl coordination. The parameters a and b are set to 3 \AA^{-1} and 3.2 \AA , respectively. The expression of N_B is given by

$$N_B = \sum_w \min(f_{\text{Na}-w}, f_{\text{Cl}-w}), \quad (7)$$

which is thereby regarded as the number of bridging water molecules.

Figure 6 shows the distribution of the committor p_B^* dataset on the two-dimensional surfaces using the combinations

(G_{58}^5, ρ) (a), (G_{1217}^5, ρ) (b), (G_{58}^5, N_B) (c), and (G_{1217}^5, N_B) (d). For each combination of variables, the corresponding correlation coefficient r was calculated and is presented in Fig. 6.

The interionic water density ρ shows a positive correlation with G_{58}^5 and a weak negative correlation with G_{1217}^5 . Note that the low sensitivity of G_{58}^5 to angular components coincides with the fact that ρ does not account for the orientation of water molecules. The two-dimensional PMF using (r_{ion}, ρ), reported in Ref. 50, indicates that an increase in ρ promotes dissociation from the associated state. This behavior is also consistent with the separatrix line described in Fig. 5(a), which indicates the increase in G_{58}^5 facilitates the ion dissociation process.

In contrast, the number of bridging water molecules N_B exhibits a positive correlation with G_{58}^5 , while its correlation with G_{1217}^5 is slightly stronger than that of ρ . Note that a water molecule must adopt an appropriate orientation to contribute to both N_B and G_{1217}^5 . The two-dimensional PMF using (r_{ion}, N_B), reported in Ref. 50, suggests the existence of multiple transition pathways: each pathway corresponds to $N_B=0, 1$, or 2 , and as N_B increases, the r_{ion} occupying the TSs decrease to approximately 4.2, 3.9, and 3.6, Å, respectively. However, as shown in Fig. 5, such multiple pathways cannot be directly identified from G_{58}^5 and G_{1217}^5 . This is due to the discrete nature of N_B , which is effectively coarse-grained when represented by ACSFs. Nevertheless, the correlations shown in Fig. 6 indicates that both ACSFs, G_{58}^5 and G_{1217}^5 , effectively represent the hand-crafted CV that describe the water bridging structure between ions.

IV. CONCLUSIONS

In this study, we identified the RC for the NaCl ion dissociation–association process using deep learning with the committor p_B^* as the training target. The committor p_B^* values were obtained by initial configurations obtained via umbrella sampling constrained along the interionic distance r_{ion} , followed by 1 ps MD trajectories. To describe the solvent environment around the ions, we introduced ACSFs, G^2 and G^5 , as CVs and used as input variables to the neural network. The model was trained by minimizing the cross entropy so that the relationship between p_B^* and the RC q followed the sigmoidal function, $p_B(q) = (1 + \tanh(q))/2$.

To interpret the resulting RC q , we applied SHAP, an XAI technique. This analysis revealed that the ACSF descriptors, G_{58}^5 and G_{1217}^5 , characterizing the water O atom environment around Na ion and the water O atoms within the hydration shell of Na and Cl ions, respectively make dominant contributions to the RC. Notably, the SHAP analysis highlights G_{58}^5 as a dominant descriptor, in agreement with the governing relationship identified by the symbolic regression analysis.²⁸ This consistency supports the physical relevance of the learned functional form for the RC. Importantly, the functional form described by the symbolic regression analysis is consistent with the input features identified by SHAP, providing mutual validation between the two analyses. Additionally, the SHAP analysis clarified that G_{1217}^5 , characterizing the O

atoms within the hydration shells of Na and Cl, also makes a dominant contribution, which has not been emphasized in prior studies. We further demonstrated that these two ACSF descriptors effectively capture the water bridging structure essential to ion dissociation, as evidenced by their correlations with conventionally defined CVs such as the interionic water density ρ and number of bridging water molecules N_B .⁵⁰

Although, as outlined in the Introduction, Ballard and Delgado showed that the inclusion of the third solvation shell is required to accurately reproduce a committor distribution peaked around p_B^* ,⁴⁹ G_{58}^5 and G_{1217}^5 contains information only for water molecules in the first solvation shell. Our candidate CVs included ACSFs with distance sensitivity up to $R_s = 9.0$ Å, approximately corresponding to the third hydration shell, but these descriptors were not identified by SHAP as major contributors. This suggests that rearrangements of water molecules in the first hydration shell effectively incorporates the influence of the second and third coordination shells.

The RC obtained through our integrated approach, which combines committor based deep learning, ACSF descriptors, and XAI, provides a refined molecular picture of solvent effects. Moreover, this methodology offers a general strategy applicable to a wide range of condensed phase reactions in which solvent reorganization plays a crucial role. It can be extended to processes such as ligand binding, nucleation, and biomolecular conformational changes, where the solvent environment significantly influence the TS.

SUPPLEMENTARY MATERIAL

The supplementary material includes figures showing the epoch dependent loss functions for training and test datasets (Fig. S1) as well as the distribution of committor p_B^* within the range $|q| < \alpha$, where α is used as the threshold (Fig. S2). It also provides a CSV file containing the definitions of input variables and those ACSF parameters, reference atom i , Z_i , Z_2 , R_s , λ , and ζ (Tables S1).

ACKNOWLEDGMENTS

The authors acknowledge Professors Yasutaka Kitagawa, Ryohei Kishi, and Kento Kasahara for valuable comments. This work was supported by JSPS KAKENHI Grant-in-Aid Grant Nos. JP23K23858, JP25H02299, JP23K23303, JP23KK0254, JP24K21756, JP25H02464, JP25K02235, JP25K00968, JP24H01719, JP22K03550, and JP23H02622. We acknowledge support from the Fugaku Supercomputing Project (Nos. JPMXP1020230325 and JPMXP1020230327) and the Data-Driven Material Research Project (No. JPMXP1122714694) from the Ministry of Education, Culture, Sports, Science, and Technology and by Maruho Collaborative Project for Theoretical Pharmaceutics. The numerical calculations were performed at Research Center of Computational Science, Okazaki Research Facilities,

National Institutes of Natural Sciences (Projects: 25-IMS-C052, 25-IMS-C105, 25-IMS-C227).

AUTHOR DECLARATIONS

CONFLICT OF INTEREST

The authors have no conflicts to disclose.

DATA AVAILABILITY STATEMENT

The data that support the findings of this study are available from the corresponding author upon reasonable request.

- ¹C. Chipot, A. Pohorille, A. W. Castleman, J. P. Toennies, K. Yamanouchi, and W. Zinth, eds., *Free Energy Calculations: Theory and Applications in Chemistry and Biology* (Springer, Berlin, Heidelberg, 2007).
- ²D. M. Zuckerman, *Statistical Physics of Biomolecules: An Introduction* (CRC Press, Boca Raton, FL, 2010).
- ³B. Peters, *Reaction Rate Theory and Rare Events* (Elsevier, Amsterdam, 2017).
- ⁴F. Pietrucci, "Strategies for the exploration of free energy landscapes: Unity in diversity and challenges ahead," *Rev. Phys.* **2**, 32–45 (2017).
- ⁵V. S. Pande, A. Y. Grosberg, T. Tanaka, and D. S. Rokhsar, "Pathways for protein folding: Is a new view needed?" *Curr. Opin. Struct. Biol.* **8**, 68–79 (1998).
- ⁶P. G. Bolhuis, C. Dellago, and D. Chandler, "Reaction coordinates of biomolecular isomerization," *Proc. Natl. Acad. Sci. U.S.A.* **97**, 5877–5882 (2000).
- ⁷P. G. Bolhuis, D. Chandler, C. Dellago, and P. L. Geissler, "TRANSITION PATH SAMPLING: Throwing Ropes Over Rough Mountain Passes, in the Dark," *Annu. Rev. Phys. Chem.* **53**, 291–318 (2002).
- ⁸G. Hummer, "From transition paths to transition states and rate coefficients," *J. Chem. Phys.* **120**, 516–523 (2004).
- ⁹R. B. Best and G. Hummer, "Reaction coordinates and rates from transition paths," *Proc. Natl. Acad. Sci. U.S.A.* **102**, 6732–6737 (2005).
- ¹⁰W. E. W. Ren, and E. Vanden-Eijnden, "Transition pathways in complex systems: Reaction coordinates, isocommittor surfaces, and transition tubes," *Chem. Phys. Lett.* **413**, 242–247 (2005).
- ¹¹H. Jung, K.-i. Okazaki, and G. Hummer, "Transition path sampling of rare events by shooting from the top," *J. Chem. Phys.* **147**, 152716 (2017).
- ¹²J. Rogal, "Reaction coordinates in complex systems—a perspective," *Eur. Phys. J. B* **94**, 223 (2021).
- ¹³P. G. Bolhuis and D. W. H. Swenson, "Transition Path Sampling as Markov Chain Monte Carlo of Trajectories: Recent Algorithms, Software, Applications, and Future Outlook," *Adv. Theory Simul.* **4**, 2000237 (2021).
- ¹⁴W. Li and A. Ma, "Recent Developments in Methods for Identifying Reaction Coordinates," *Mol. Simul.* **40**, 784–793 (2014).
- ¹⁵A. Ma and A. R. Dinner, "Automatic Method for Identifying Reaction Coordinates in Complex Systems," *J. Phys. Chem. B* **109**, 6769–6779 (2005).
- ¹⁶B. Peters and B. L. Trout, "Obtaining reaction coordinates by likelihood maximization," *J. Chem. Phys.* **125**, 054108 (2006).
- ¹⁷B. Peters, G. T. Beckham, and B. L. Trout, "Extensions to the likelihood maximization approach for finding reaction coordinates," *J. Chem. Phys.* **127**, 034109 (2007).
- ¹⁸B. Peters, "Reaction Coordinates and Mechanistic Hypothesis Tests," *Annu. Rev. Phys. Chem.* **67**, 669–690 (2016).
- ¹⁹E. Schneider, L. Dai, R. Q. Topper, C. Drechsel-Grau, and M. E. Tuckerman, "Stochastic Neural Network Approach for Learning High-Dimensional Free Energy Surfaces," *Phys. Rev. Lett.* **119**, 150601 (2017).
- ²⁰J. Rogal, E. Schneider, and M. E. Tuckerman, "Neural-Network-Based Path Collective Variables for Enhanced Sampling of Phase Transformations," *Phys. Rev. Lett.* **123**, 245701 (2019).
- ²¹Y. Mori, K.-i. Okazaki, T. Mori, K. Kim, and N. Matubayasi, "Learning reaction coordinates via cross-entropy minimization: Application to alanine dipeptide," *J. Chem. Phys.* **153**, 054115 (2020).
- ²²L. Bonati, V. Rizzi, and M. Parrinello, "Data-Driven Collective Variables for Enhanced Sampling," *J. Phys. Chem. Lett.* **11**, 2998–3004 (2020).
- ²³L. Bonati, G. Piccini, and M. Parrinello, "Deep learning the slow modes for rare events sampling," *Proc. Natl. Acad. Sci. U.S.A.* **118**, e2113533118 (2021), arXiv:2107.03943.
- ²⁴M. Frassek, A. Arjun, and P. G. Bolhuis, "An extended autoencoder model for reaction coordinate discovery in rare event molecular dynamics datasets," *J. Chem. Phys.* **155**, 064103 (2021).
- ²⁵T. Magrino, L. Huet, A. M. Saitta, and F. Pietrucci, "Critical Assessment of Data-Driven versus Heuristic Reaction Coordinates in Solution Chemistry," *J. Phys. Chem. A* **126**, 8887–8900 (2022).
- ²⁶J. Neumann and N. Schwierz, "Artificial Intelligence Resolves Kinetic Pathways of Magnesium Binding to RNA," *J. Chem. Theory Comput.* **18**, 1202–1212 (2022).
- ²⁷G. Lazzeri, H. Jung, P. G. Bolhuis, and R. Covino, "Molecular Free Energies, Rates, and Mechanisms from Data-Efficient Path Sampling Simulations," *J. Chem. Theory Comput.* **19**, 9060–9076 (2023).
- ²⁸H. Jung, R. Covino, A. Arjun, C. Leitold, C. Dellago, P. G. Bolhuis, and G. Hummer, "Machine-guided path sampling to discover mechanisms of molecular self-organization," *Nat. Comput. Sci.* **3**, 334–345 (2023).
- ²⁹H. Chen, B. Roux, and C. Chipot, "Discovering Reaction Pathways, Slow Variables, and Commitor Probabilities with Machine Learning," *J. Chem. Theory Comput.* **19**, 4414–4426 (2023).
- ³⁰N. Naleem, C. R. A. Abreu, K. Warmuz, M. Tong, S. Kirmizialtin, and M. E. Tuckerman, "An exploration of machine learning models for the determination of reaction coordinates associated with conformational transitions," *J. Chem. Phys.* **159**, 034102 (2023).
- ³¹A. France-Lanord, H. Vroylandt, M. Salanne, B. Rotenberg, A. M. Saitta, and F. Pietrucci, "Data-Driven Path Collective Variables," *J. Chem. Theory Comput.* **20**, 3069–3084 (2024).
- ³²J. Zhang, L. Bonati, E. Trizio, O. Zhang, Y. Kang, T. Hou, and M. Parrinello, "Descriptor-Free Collective Variables from Geometric Graph Neural Networks," *J. Chem. Theory Comput.* **20**, 10787–10797 (2024).
- ³³N. S. M. Herringer, S. Dasetty, D. Gandhi, J. Lee, and A. L. Ferguson, "Permutationally Invariant Networks for Enhanced Sampling (PINES): Discovery of Multimolecular and Solvent-Inclusive Collective Variables," *J. Chem. Theory Comput.* **20**, 178–198 (2024).
- ³⁴K. Zhu, E. Trizio, J. Zhang, R. Hu, L. Jiang, T. Hou, and L. Bonati, "Enhanced Sampling in the Age of Machine Learning: Algorithms and Applications," *Chem. Rev.*, acs.chemrev.5c00700 (2025).
- ³⁵A. Megías, S. Contreras Arredondo, C. G. Chen, C. Tang, B. Roux, and C. Chipot, "Iterative variational learning of committor-consistent transition pathways using artificial neural networks," *Nat. Comput. Sci.* **5**, 592–602 (2025).
- ³⁶F. M. Dietrich and M. Salvalaglio, "On the reproducibility of free energy surfaces in machine-learned collective variable spaces," *J. Chem. Phys.* **163**, 141102 (2025).
- ³⁷T. Kikutsuji, Y. Mori, K.-i. Okazaki, T. Mori, K. Kim, and N. Matubayasi, "Explaining reaction coordinates of alanine dipeptide isomerization obtained from deep neural networks using Explainable Artificial Intelligence (XAI)," *J. Chem. Phys.* **156**, 154108 (2022).
- ³⁸K. Okada, T. Kikutsuji, K.-i. Okazaki, T. Mori, K. Kim, and N. Matubayasi, "Unveiling interatomic distances influencing the reaction coordinates in alanine dipeptide isomerization: An explainable deep learning approach," *J. Chem. Phys.* **160**, 174110 (2024).
- ³⁹K. Kawashima, T. Sato, K.-i. Okazaki, K. Kim, N. Matubayasi, and T. Mori, "Investigating the hyperparameter space of deep neural network models for reaction coordinates," *APL Mach. Learn.* **3**, 016113 (2025).
- ⁴⁰O. A. Karim and J. Andrew. McCammon, "Dynamics of a sodium chloride ion pair in water," *J. Am. Chem. Soc.* **108**, 1762–1766 (1986).
- ⁴¹O. A. Karim and J. A. McCammon, "Rate constants for ion pair formation and dissociation in water," *Chem. Phys. Lett.* **132**, 219–224 (1986).
- ⁴²G. Ciccotti, M. Ferrario, J. T. Hynes, and R. Kapral, "Constrained molecular dynamics and the mean potential for an ion pair in a polar solvent," *Chem. Phys.* **129**, 241–251 (1989).
- ⁴³G. Ciccotti, M. Ferrario, J. T. Hynes, and R. Kapral, "Dynamics of ion pair interconversion in a polar solvent," *J. Chem. Phys.* **93**, 7137–7147 (1990).

- ⁴⁴E. Guàrdia, R. Rey, and J. A. Padró, "Potential of mean force by constrained molecular dynamics: A sodium chloride ion-pair in water," *Chem. Phys.* **155**, 187–195 (1991).
- ⁴⁵R. Rey and E. Guardia, "Dynamical aspects of the sodium(1+)-chloride ion pair association in water," *J. Phys. Chem.* **96**, 4712–4718 (1992).
- ⁴⁶D. E. Smith and L. X. Dang, "Computer simulations of NaCl association in polarizable water," *J. Chem. Phys.* **100**, 3757–3766 (1994).
- ⁴⁷F. N. Brüning, J. O. Daldrop, and R. R. Netz, "Pair-Reaction Dynamics in Water: Competition of Memory, Potential Shape, and Inertial Effects," *J. Phys. Chem. B* **126**, 10295–10304 (2022).
- ⁴⁸P. L. Geissler, C. Dellago, and D. Chandler, "Kinetic Pathways of Ion Pair Dissociation in Water," *J. Phys. Chem. B* **103**, 3706–3710 (1999).
- ⁴⁹A. J. Ballard and C. Dellago, "Toward the Mechanism of Ionic Dissociation in Water," *J. Phys. Chem. B* **116**, 13490–13497 (2012).
- ⁵⁰R. G. Mullen, J.-E. Shea, and B. Peters, "Transmission Coefficients, Committers, and Solvent Coordinates in Ion-Pair Dissociation," *J. Chem. Theory Comput.* **10**, 659–667 (2014).
- ⁵¹Y. Yonetani, "Distinct dissociation kinetics between ion pairs: Solvent-coordinate free-energy landscape analysis," *J. Chem. Phys.* **143**, 044506 (2015).
- ⁵²Y. Yonetani, "Solvent-coordinate free-energy landscape view of water-mediated ion-pair dissociation," *Mol. Phys.* **115**, 2987–2998 (2017).
- ⁵³M. Salanne, S. Tazi, R. Vuilleumier, and B. Rotenberg, "Ca²⁺-Cl⁻ Association in Water Revisited: The Role of Cation Hydration," *ChemPhysChem* **18**, 2807–2811 (2017).
- ⁵⁴M. N. Joswiak, M. F. Doherty, and B. Peters, "Ion dissolution mechanism and kinetics at kink sites on NaCl surfaces," *Proc. Natl. Acad. Sci. U.S.A.* **115**, 656–661 (2018).
- ⁵⁵M. I. Oh, M. Gupta, and D. F. Weaver, "Understanding Water Structure in an Ion-Pair Solvation Shell in the Vicinity of a Water/Membrane Interface," *J. Phys. Chem. B* **123**, 3945–3954 (2019).
- ⁵⁶C. Zhang, F. Giberti, E. Sevgen, J. J. de Pablo, F. Gygi, and G. Galli, "Dissociation of salts in water under pressure," *Nat. Commun.* **11**, 3037 (2020).
- ⁵⁷D. Wang, R. Zhao, J. D. Weeks, and P. Tiwary, "Influence of Long-Range Forces on the Transition States and Dynamics of NaCl Ion-Pair Dissociation in Water," *J. Phys. Chem. B* **126**, 545–551 (2022).
- ⁵⁸K. Wilke, S. Tao, S. Calero, A. Lervik, and T. S. van Erp, "NaCl Dissociation Explored Through Predictive Power Path Sampling Analysis," *J. Chem. Theory Comput.* **21**, 4604–4614 (2025).
- ⁵⁹B. Peters, "Inertial likelihood maximization for reaction coordinates with high transmission coefficients," *Chem. Phys. Lett.* **554**, 248–253 (2012).
- ⁶⁰J. Behler and M. Parrinello, "Generalized Neural-Network Representation of High-Dimensional Potential-Energy Surfaces," *Phys. Rev. Lett.* **98**, 146401 (2007).
- ⁶¹J. Behler, "Atom-centered symmetry functions for constructing high-dimensional neural network potentials," *J. Chem. Phys.* **134**, 074106 (2011).
- ⁶²J. Behler, "Perspective: Machine learning potentials for atomistic simulations," *J. Chem. Phys.* **145**, 170901 (2016).
- ⁶³S. M. Lundberg and S.-I. Lee, "A unified approach to interpreting model predictions," in *Proceedings of the 31st international conference on neural information processing systems* (Curran Associates Inc., Red Hook, NY, 2017) pp. 4768–4777.
- ⁶⁴J. Wang, P. Cieplak, and P. A. Kollman, "How well does a restrained electrostatic potential (RESP) model perform in calculating conformational energies of organic and biological molecules?" *J. Comput. Chem.* **21**, 1049–1074 (2000).
- ⁶⁵H. W. Horn, W. C. Swope, J. W. Pitera, J. D. Madura, T. J. Dick, G. L. Hura, and T. Head-Gordon, "Development of an improved four-site water model for biomolecular simulations: TIP4P-Ew," *J. Chem. Phys.* **120**, 9665–9678 (2004).
- ⁶⁶M. J. Abraham, T. Murtola, R. Schulz, S. Páll, J. C. Smith, B. Hess, and E. Lindahl, "GROMACS: High performance molecular simulations through multi-level parallelism from laptops to supercomputers," *SoftwareX* **1–2**, 19–25 (2015).
- ⁶⁷T. Mori and S. Saito, "Dissecting the Dynamics during Enzyme Catalysis: A Case Study of Pin1 Peptidyl-Prolyl Isomerase," *J. Chem. Theory Comput.* **16**, 3396–3407 (2020).
- ⁶⁸P. Geiger and C. Dellago, "Neural networks for local structure detection in polymorphic systems," *J. Chem. Phys.* **139**, 164105 (2013).
- ⁶⁹R. S. DeFever, C. Targonski, S. W. Hall, M. C. Smith, and S. Sarupria, "A generalized deep learning approach for local structure identification in molecular simulations," *Chem. Sci.* **10**, 7503–7515 (2019).
- ⁷⁰M. Fulford, M. Salvalaglio, and C. Molteni, "DeepIce: A Deep Neural Network Approach To Identify Ice and Water Molecules," *J. Chem. Inf. Model.* **59**, 2141–2149 (2019).
- ⁷¹Y. Matsunaga, M. Kamiya, H. Oshima, J. Jung, S. Ito, and Y. Sugita, "Use of multistate Bennett acceptance ratio method for free-energy calculations from enhanced sampling and free-energy perturbation," *Biophys. Rev.* **14**, 1503–1512 (2022).
- ⁷²J. Jung, T. Mori, C. Kobayashi, Y. Matsunaga, T. Yoda, M. Feig, and Y. Sugita, "GENESIS: A hybrid-parallel and multi-scale molecular dynamics simulator with enhanced sampling algorithms for biomolecular and cellular simulations," *WIREs Comput. Mol. Sci.* **5**, 310–323 (2015).
- ⁷³C. Kobayashi, J. Jung, Y. Matsunaga, T. Mori, T. Ando, K. Tamura, M. Kamiya, and Y. Sugita, "GENESIS 1.1: A hybrid-parallel molecular dynamics simulator with enhanced sampling algorithms on multiple computational platforms," *J. Comput. Chem.* **38**, 2193–2206 (2017).
- ⁷⁴J. Jung, K. Yagi, C. Tan, H. Oshima, T. Mori, I. Yu, Y. Matsunaga, C. Kobayashi, S. Ito, D. Ugarte La Torre, and Y. Sugita, "GENESIS 2.1: High-Performance Molecular Dynamics Software for Enhanced Sampling and Free-Energy Calculations for Atomistic, Coarse-Grained, and Quantum Mechanics/Molecular Mechanics Models," *J. Phys. Chem. B* **128**, 6028–6048 (2024).
- ⁷⁵M. R. Shirts and J. D. Chodera, "Statistically optimal analysis of samples from multiple equilibrium states," *J. Chem. Phys.* **129**, 124105 (2008).

Supplementary Material

Deep learning of committor for ion dissociation and interpretable analysis of solvent effects using atom-centered symmetry functions

Kenji Okada,¹ Kazushi Okada,¹ Kei-ichi Okazaki,^{2,3} Toshifumi Mori,^{4,5} Kang Kim,¹ and Nobuyuki Matubayasi¹

¹*Division of Chemical Engineering, Graduate School of Engineering Science, The University of Osaka, Osaka 560-8531, Japan*

²*Research Center for Computational Science, Institute for Molecular Science, Okazaki, Aichi 444-8585, Japan*

³*Graduate Institute for Advanced Studies, SOKENDAI, Okazaki, Aichi 444-8585, Japan*

⁴*Institute for Materials Chemistry and Engineering, Kyushu University, Kasuga, Fukuoka 816-8580, Japan*

⁵*Interdisciplinary Graduate School of Engineering Sciences, Kyushu University, Kasuga, Fukuoka 816-8580, Japan*

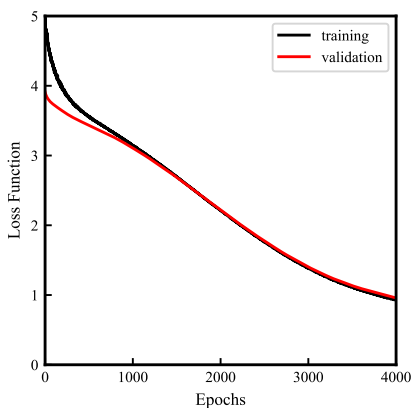


FIG. S1. Epoch dependent loss functions of training and test datasets.

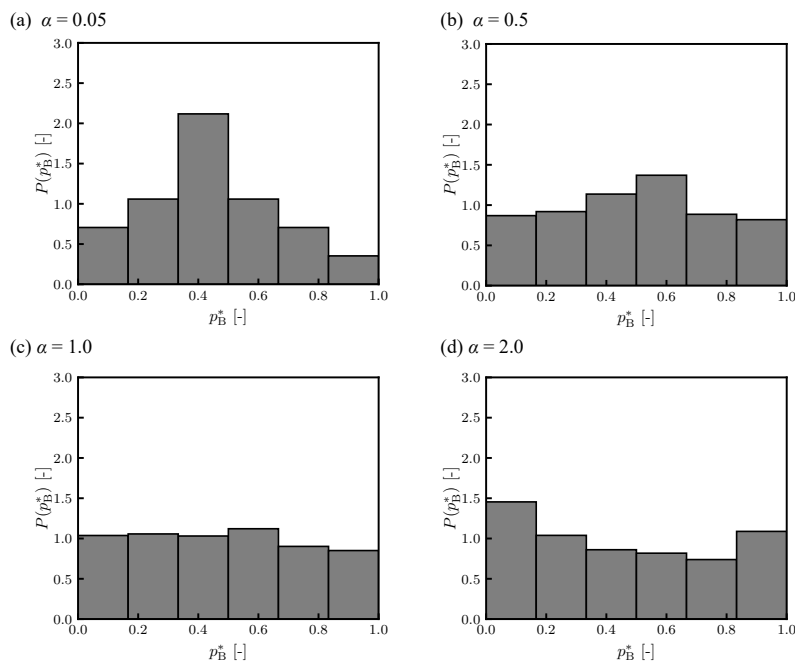


FIG. S2. Probability density of committor p_B^* within the range $|q| < \alpha$ with the threshold values, $\alpha = 0.05$ (a), 0.5 (b), 1.0 (c), and 2.0 (d).